Wireless Channel for 6th Generation Networks Sensing

Erik Fredenvall, Gustaf Ferm, Maria Obaitan,
Albin Bjärkby, Jacob Fagerstål

Group: EENX16-VT25-34

May 13, 2025

Abstract

This thesis investigates the potential of using S_{21} parameter data for human presence detection in indoor wireless environments, as part of early research related to 6th generation (6G) communication systems. By combining physical measurements from a vector network analyzer with simulations generated using a digital twin of Chalmers' antenna lab in Ansys HFSS, the study evaluates signal behavior across the 4–40 GHz frequency range. Power-Angle-Delay Profiles (PADPs) were created to visualize signal propagation and identify human-induced reflections. A feed-forward neural network was trained on both measured and simulated S_{21} data to classify human presence. The network achieved high classification accuracy when trained and tested on data from the same environment and on combined data, while cross-environment testing revealed a significant drop in performance, likely due to differences between simulated and real environments. Additionally, frequency slicing and link budget analysis were used to recommend suitable frequency bands for indoor sensing. The findings indicate that a lower-range band around 5 GHz offers a good signal-to-noise ratio and maintains the main features of the signal. The study provides a proof of concept for RF-based human sensing using communication signals and offers insights into simulation accuracy, neural network training, and future development of 6G human-aware systems.

Contents

1 Introduction

1.1 Background

While 5G is widespread and commonly used today, the sixth generation (6G) is being investigated as the next step in wireless communication. Building on the foundation of its predecessors, the aim of 6G is to provide ultra-reliable, low-latency and high-speed communication [1]. Researchers at Chalmers antenna group are at the frontier in this field and this project aims to gather valuable data that could help in this research. An important aspect of this research is try to evaluate different frequency ranges in which 6G could operate. In addition, as a potential part of future traffic safety, properties like the amplitude and phase of a communications signal could be used to localize and identify a human. This is not possible with today's technology, instead, cars currently only use radar to scan the surrounding environment. The 6G human sensing would operate through analyzing how the received signal is altered when something passes through the signal path. For this to work, it is essential that devices and base stations can detect and decode differences in the signal path to be able to differentiate between if a human or an object is present. The signal path between the transmitting and receiving antennas on the devices can be described using the S_{21} parameter [2].

As of today, the channel state information (CSI) is used in many aspects of modern communication systems, for example:

- Wireless Localization & Positioning
- Channel Estimation & Equalization in Signal Processing
- Wireless Security & Authentication
- Handover & Mobility Management
- Interference Mitigation & Dynamic Spectrum Allocation

There are multiple ways to describe, visualize and analyze wireless channels. Central to these are scattering parameters, also known as S-parameters, these describe how signals are reflected and transmitted in a multiport network. To then visualize the signal, power-angle delay profiles (PAPD) can be used to determine the strength and direction of a received signal.

The efficiency of transmissions can also be described by:

- Channel capacity, the highest possible rate of information per second while maintaining a low error probability. This depends on bandwidth and signal to noise ratio.
- Bandwidth, the range of frequencies used to transmit the signal. A higher bandwidth allows for faster transfer of information since different frequencies can be used to transport information at the same time
- Signal to noise ratio (SNR) compares the energy of the received signal with the background noise in the space [3]. A high SNR means that the signal is easy to distinguish from noise while a low SNR means the power of the signal is closer to the power to the noise, which increases the error probability.

1.2 Purpose

The desired applications in this project is to find the best frequency range for 6G to transfer data between two antennas, and to use the CSI for detecting obstacles in the signal pathway and determine if it is a human. To make it easier to provide more data, a simulation software is used.

1.3 Problem description

During the project, several aspects of wireless channels are investigated. The goal is to achieve the following points:

- To provide measurement data of power angle delay profiles for different frequency bands for indoor communication.
- To give a recommendation for at least 5 frequency bands for indoor 6G communication and sensing that are potentially interesting for future research.
- Construct a digital twin of Chalmers antenna lab in the provided simulation software.
- Confirm the viability of using the provided simulation software to generate simulated data.
- To investigate whether a simple neural network can be trained to reliably detect human presence between a transmitting and receiving antenna indoors.

1.4 Scope

Due to time constraints and available equipment, the project has the following limitations:

- The studied frequencies range from 4-40 GHz.
- Only indoor situations are considered.
- This project does not develop a fully functioning system for human presence detection, but a proof of concept.
- Only static situations are measured.

2 Theory

In this section the relevant theory that is fundamental for this project is presented.

2.1 Link budget

In order to investigate the gains and losses of a signal moving through a channel from a sender to a receiver, a link budget analysis is useful. It investigates how signal waves fade in the propagation process. The model includes the gains of the transmitting and receiving antennas, feeder cables and their related losses, free space loss, effective isotropic radiated power and propagation loss. The equation used to calculate the link budget is as follows:

$$P_{RX} = P_{TX} + G_{TX} - L_{TX} - L_{FX} - L_M + G_{RX} - L_{RX}. \tag{1}$$

Where P_{RX} (dBm) is the received power, P_{TX} (dBm) transmitted power G_{TX} and G_{RX} (dBmi) are the antenna gains, L_{TX}(dB) and L_{RX} are the transmitter and receiver losses from cables and connectors etc, L_{FS}(dB) is the free space path loss and L_M(dB) are miscellanious losses. The free space path loss is usually the most significant contribution to the total loss. It is caused by the spreading of a signal when it passes through free space. The equation for the path loss is:

$$L_{FS} = 20log_{10}\left(4\pi\frac{d}{\lambda}\right) \tag{2}$$

Where d is the covered distance and λ is the signal wavelength.

2.2 Vector Network Analyzer

A Vector Network Analyzer (VNA) is a fundamental tool in radio frequency (RF) and microwave engineering, used to measure the electrical behavior of networks and the characterization of S-parameters [4]. With a VNA, it is possible to determine key properties such as Intermediate Frequency bandwidth, frequency range and number of frequency points for a sweep. A higher number of points provides finer detail across the measured band but may require longer measurement time.

Calibration is necessary in order to handle systematic errors. Systematic errors occur in a reproducible manner due to inherent properties of the cables and the VNA. Calibration is a way to remove these errors mathematically. The interface between the cable from the VNA and the connecting device, such as an antenna is called the reference plane [5].

2.3 S-parameters

Scattering parameters, also known as S-parameters are used to describe the characteristics of an electrical network when it is being stimulated by an electrical signal [6]. The S-parameters are represented in a $n \times n$ mathematical S-matrix , where n refers to the number of input ports. Since the VNA used in this project is a 2-port device the S-matrix is defined as:

$$S = \begin{bmatrix} S_{11} & S_{12} \\ S_{21} & S_{22} \end{bmatrix} \tag{3}$$

Each parameter represents different characteristics of the electrical network.

- S_{11}- Represents the input port reflection coefficient
- S_{12} - Input port reflection coefficient, also refered to as reverse voltage gain
- S_{21} - Transmission coefficient, forward voltage gain
- S_{22} - Output port reflection coefficient

Since the S_{21} parameter presents a ratio between received signal at port 2 with respect to the transmitted signal at port one it can effectively be used to evaluate signal transmission losses through an antenna system [2].

2.4 Inverse fast Fourier transform

The inverse Fourier transform (IFFT) transforms a signal in the frequency domain into its time domain form [7]. In order to utilize fourier transforms and apply them to digital signals the digital fourier transform (DFT) has to be applied. For a discrete time signal s[n] that has a period of $T_0 = NT_s$, where T_s is the sampling interval and N represents the number of samples per period. The DFT is given by

$$S[k] = \sum_{0}^{N-1} s[n]e^{-j2\pi\frac{n}{N}k}. \tag{4}$$

The exponential term $e^{-j2\pi\frac{n}{N}k}$ is a complex phasor representation of a discrete sinusoidal function. This function only contains one frequency component which it oscillates at. Each time domain sample is multiplied with its corresponding phasor. The sum of all multiplications over all n form $0 < n < N-1$ transforms the signal into its frequency domain representation.

In a similar manner, the inverse discrete Fourier transform (IDFT) of the frequency domain signal S[k] is given by

$$s[n] = \sum_{0}^{N-1} S[k]e^{-j2\pi\frac{k}{N}n}. \tag{5}$$

It converts the discrete frequency domain signal into its time domain form. The fast Fourier transform is a faster and more efficient way of computing the DFT of a signal. The calculation algorithm is made more effective by reducing the complexity from $O(N^2)$ to $O(Nlog_2N)$ [8]. Similarly, the fast algorithm can be used to compute the IDFT, in other words, inverse fast Fourier transform (IFFT).

2.5 Windowing

Window functions are widely used in signal processing. To understand the basic functions of a window function, let x(n) be a long sequence and w(n) a window function of length N, where N is the number of samples. The purpose of the window function w(n) is to truncate the original signal x(n) into a N-point sequence $x_n(n)$ according to the following equation:

$$x_n(n) = x(n)w(n). \tag{6}$$

The process of truncating the signal is equal to multiplying the given signal with a window function, thus resulting in a finite variation of the signal [9].

In the frequency domain this translates to convolution. The truncation of a signal leads to expansion of the bandwidth resulting in spectral leakage. Though leakage is inevitable, it can be reduced by applying a window function with desired properties. Some of the desirable properties of a window function f(t), with duration 2τ and it's Fourier transform $F(j\omega)$ are:

- f(t) should be a real and non negative function.
- f(t) should attain its maximum at t=0 and f(t) = 0 for all $\mid t \mid > \tau$, where τ is the one sided duration of the window.
- $F(j\omega)$ should have a main lobe around the origin and side lobes on either side.
- The main lobe should contain the bulk of the total energy.
- The maximum side lobe level should be minimized relative to the main lobe peak level.

Examples of window functions are the Kaiser window functions. They are composed of zero-order Bessel functions. The modified zeroth-order Kaiser-Bessel window is defined by:

$$f[n] = \frac{I_0\left[\alpha\sqrt{\alpha - \left(\frac{2n}{N}\right)^2}\right]}{I_0[\alpha]} \tag{7}$$

for n in range $0 \leq \mid n \mid \leq \frac{N}{2}$. $I_0(x)$ is the modified Bessel function of zeroth order. It is defined as:

$$I_0(x) = \frac{1}{(m!)^2}\left(\frac{x}{2}\right)^{2m} \tag{8}$$

One advantage of the Kaiser windows are their flexible design. By adjusting the parameters, wanted proportions between main and side lobes can be attained [10].

2.6 Power angle delay profile

A power delay profile (PDP) gives the received power strength through a multipath channel as a function of propagation delay [11]. They are commonly used in localization based applications due to their capability of characterizing a multipath channel [12]. The time resolution, Δt of the PDP is limited by the bandwidth, B of the transmitted signal according to the relation:

$$\Delta t = \frac{1}{B}. \tag{9}$$

Similarly the power angle profile (PAP) describes the received power at each azimuth angle where ϕ_k is the azimuth angle and $P_R(\phi_k)$ is the received power at a certain angle.

$$PAP = P_R(\phi_k) = \sum_{1}^{N} P(\tau_n, \phi_k). \tag{10}$$

A power angle delay profile (PADP) combines the temporal and spatial components of the channel by integrating both PDP and PAP. As such it gives a comprehensive view of how signal power varies with distance and angle.

2.7 Neural network

A neural network is a type of machine learning model inspired by the structure of the human brain. It consists of interconnected units called neurons, making it capable of learning complex patterns and functions from data. Neurons are organized into layers with each neuron being connected to neurons in the subsequent layer. They are connected through weights which are parameters used in training to minimize the errors. Every layer between the input and output layers are called hidden layers [13][14][15]. An illustration of how a neural network operates to determine a human presence is shown in figure 1 below.

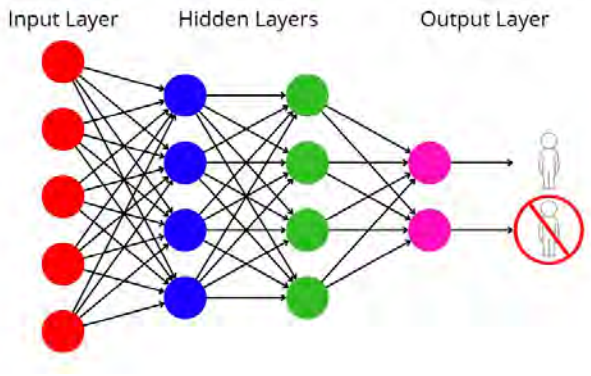

Figure 1: Basic neural network

A key algorithm used to train neural networks is backpropagation, which adjusts weights based on the error gradient. Another training process used is a learning algorithm. This uses the gradient descent and its variants, which optimize the weights to reduce prediction error. In this project the learning algorithm Adam was used. Adam is short for Adaptive Moment Estimation and uses estimates of the gradient's first and second moments to adaptively scale the learning rate for each parameter [13][15][16].

There are different types of neural networks that are used for different types of learning. In this project, a feedforward fully connected neural network was used. A feedforward neural network (FNN) is the simplest type of network where the information flows in one direction, from input to output. It is used for tasks like classification and regression [17].

When training a neural network, different parameters can be modified to optimize the training outcome. The number of epochs and learning rate. Epochs refer to how many times the entire training dataset is passed through the network. Learning rate determines the size of the steps the optimizer takes to minimize the loss function [18].

In this project, PyTorch was used to build the FNN. PyTorch is a commonly used machine learning library made by Facebook. For python users, it is easy to learn and has good flexibility in model building making it suitable for research. [19]

3 Methodology

In order to investigate the research aims, this study implemented experimental methods that will be explained in this section.

3.1 Lab measurements

All physical measurements were made in the THz lab at Chalmers. The measurement setup included a pair of vertically polarized antennas, a transmitter (Tx) and a receiver (Rx) placed on a rotating table as seen in Figure 2.

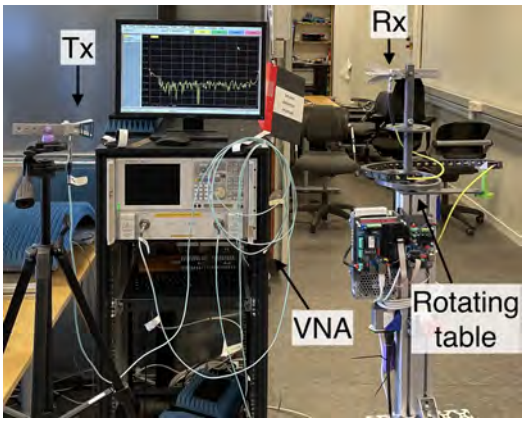

Figure 2: Measurement setup in the THz lab at Chalmers.

The Tx antenna used in this project was a double rigged horn antenna and the Rx antenna was a quad rigged horn antenna which can be seen in figure 3 and 4. The shape of the antennas promotes broadband measurements.

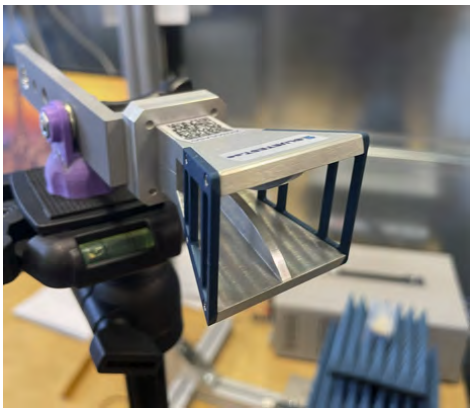

Figure 3: Transmitting antenna

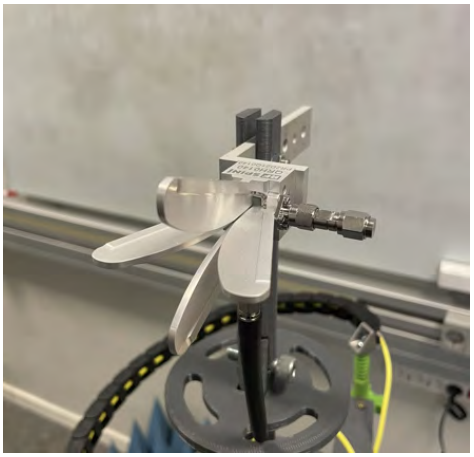

Figure 4: Receiving antenna

The antennas were connected to the VNA with cables. Before doing any measurements a calibration of the VNA was done. All systematic errors that come before the calibration plane are accounted for during calibration. Each calibration was done by doing a short, open, broadband load and a through measurement at the reference plane, which was at the cable ends with attached adapters. The block diagram of the measurement setup can be seen in figure 5 and the material specifications in table 1.

Table 1: Equipments for the lab measurements

Equipment	Name	Range
VNA	Agilent E8363B	10 MHz to 40 GHz
Transmitting antenna	DRH50 from RF SPIN	3 GHz to 40 GHz
Receiving antenna	QRH0140 from RF SPIN	4 GHz to 40 GHz
Rotating table	Custom-made	$0° - 360°$

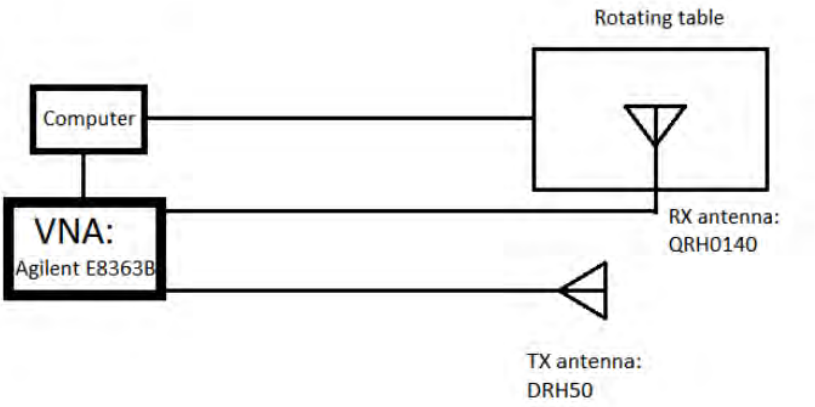

Figure 5: Block diagram of the lab measurement set up

Calculations and measurements were made to determine the link budget and to check if the signal losses were too big in the higher frequency range. Due to higher losses in the range 30-40 GHz, all measurement were made in the range 4-30 GHz.

3.1.1 Measurements for PADP

In order to gather data for the PADPs a series of measurements were made. For these measurements the VNA had the following settings:

- Frequency points: 2601
- IF Bandwidth: 10 kHz/1 kHz
- Power: 3 dBm (max output power)

The bandwidth of 10 kHz was tested at first to decrease measurement time. To achieve good enough SNR to distinguish the wanted features in the PADP, this value was adjusted to 1 kHz. The height of the Tx and Rx antennas was set up to be 140 cm from the ground. Additional adapters were placed at the cable ends in order to protect the VNA and antenna ports from mechanical damage.

Each measurement was done with a rotaton from 0° to 360° with a 15° degree angle step through use of a programmable rotating table, visible in figure 2. These broadband measurements were conducted at frequency sweeps from 4-30 GHz, providing a 26 GHz bandwidth. For these measurements a set of different setups were used, including LOS and NLOS. The distance between, and position of, the Tx and Rx antennas were varied between the measurements. For each setup a measurement was conducted both with and without a human being present in the signal path. A total of one hundred different measurements were conducted to collect data for the PADPs.

The PADPs were built by post processing the data of the S_{21} parameter from the measurements. Before applying a IFFT a Kaiser window function was applied across the frequency domain data. The windowed S_{21} data was then transformed into the time domain by doing an IFFT along the frequency axis. For each angle, all of the frequency points were plotted with their corresponding power level. Thus resulting in a PADP with distance on the horizontal axis, the receiver angle on the vertical axis and power level visualized with a color map. In order to estimate the communication quality from the PADPs the data set was sliced into relatively narrow bands with 0.4 GHz bandwidth. The slicing was made in the low, medium and high frequencies at 5, 14 and 26 GHz. The signal to noise ratio (SNR) in the different frequency bands can be used to compare the different frequency bands. The intensity and number of power peaks as well as the amount of noise that are visualized in the PADPs can be used as a metric to compare the different frequency bands.

In order to investigate the human presence detection, similar measurements were done but with an additional human placed in the setup in order to affect the signal. All human presence detection measurements were conducted under static conditions.

3.1.2 Measurements for Neural Network

In order to provide measurement data for the neural network the lab measurements were simplified. These simplified measurements were made with frequency sweeps from 4 to 30 GHz and an angle sweep from 0° to 30° degrees with 15° angle steps. For these measurements the antennas remained in the same spot. To obtain a balanced data set, fifty measurements were conducted with, and fifty without a human.

The non-human measurement were made by adjusting the placement of objects in the lab environment such as chairs and other furniture. Half of the measurements with human presence were made by varying the position of the human, both in between the direct path and besides it. The other half were conducted in a similar way with additional chairs being placed in the signal path. All of the measurements that were made for the neural network were LOS measurements. These measurements were not postprocessed into PADPs but were purely made to train the neural network.

3.2 Simulation

To enable simulated measurements suitable for comparison with empirical data, a digital twin of the Chalmers Antenna Laboratory was developed. The modelling and simulation tasks were carried out using ANSYS HFSS SBR+, an asymptotic high-frequency electromagnetic solver specifically designed for the analysis of electrically large environments where conventional full-wave methods are too slow due to heavier computation load. HFSS SBR+ employs the Shooting and Bouncing Ray (SBR) technique, augmented with advanced diffraction models (including the Physical Theory of Diffraction (PTD), Uniform Theory of Diffraction (UTD), and Creeping Wave (CW) physics) to provide accurate and efficient electromagnetic field predictions [20].

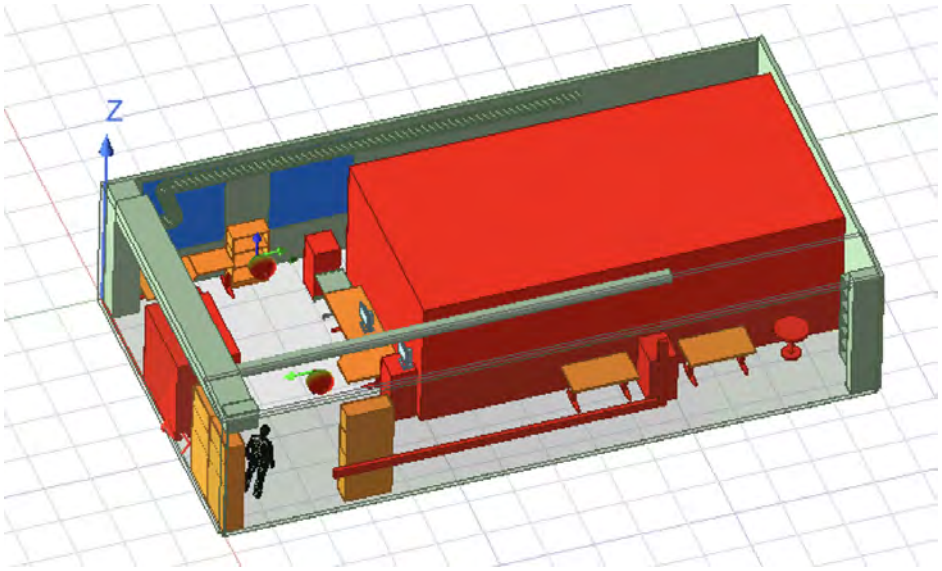

Figure 6: The digital twin in ANSYS HFSS with transmitting antenna, receiving antenna and a human.

The digital twin focused primarily on replicating large-scale structures such as tables, boxes, and shelves, as illustrated in Figure 6. Complex furniture components, such as table legs and shelving units, were designed in AutoCAD and subsequently imported into HFSS. All measurements of the furniture and the lab itself were made with a Bosch laser measurement tool with an uncertainty of ± 2 mm. Due to the computational demands of the simulations, a dedicated server was allocated to ensure uninterrupted processing over extended periods.

Experiments were made with different parameters to find the best trade-off between accuracy in the simulation compared to the real-life measurements, and simulation time. Parameters such as the frequency span and resolution were matched to those used in the physical experiments, specifically 4–30 GHz with 10 MHz frequency steps. Other parameters that were specific to the simulation were ray density and bounces. Ray density can be explained as how many rays were produced by the transmitting antenna. Bounces is the number of times a given ray will be reflected on different materials before the signal is considered to have an amplitude equal to zero. These two parameters were important because they had a big impact on the simulation time as well as the accuracy of the measurement. The resulting S_{21} parameter data was visualized in a PADP (Power-Angle-Delay Profile) and compared to corresponding real-world measurements. If the human presence in the simulation's PADP resembled that in the actual measurements, the configuration was deemed sufficiently accurate.

3.3 Settings on the simulation software

Figure 7 and Figure 8 show the same antenna setup with and without the presence of a human, respectively. Different ray density settings in HFSS SBR+ were used in the simulations, along with the corresponding simulation runtimes. The runtimes differed for the same setups but was used as an approximation of how long many setups would take to simulate. Every setup was simulated with and without a human and compared to lab measurements and evaluated if the accuracy due to ray density was enough to recognize the human presence in the PADPs.

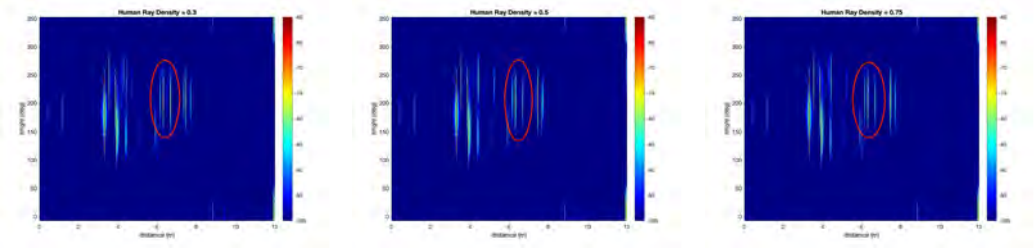

(a) Ray density = 0.3
Time ≈ 2.5 h

(b) Ray density = 0.5
Time ≈ 5.5 h

(c) Ray density = 0.75
Time ≈ 11 h

Figure 7: Power Angle Delay Profiles at ray density Human Simulated

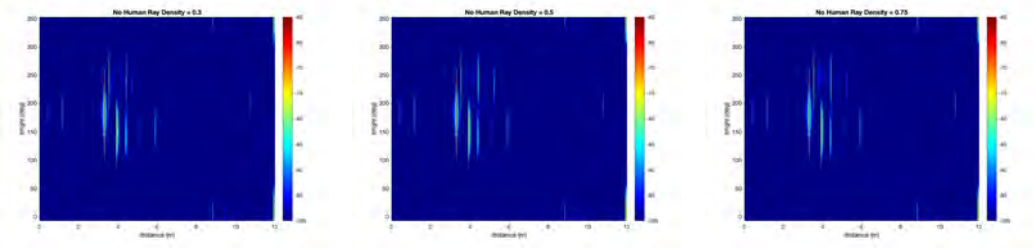

(a) Ray density = 0.3
Time ≈ 2.5 h

(b) Ray density = 0.5
Time ≈ 5.5 h

(c) Ray density = 0.75
Time ≈ 11 h

Figure 8: Power Angle Delay Profiles at ray density No Human Simulated

Figure 7a shows that a human can be seen in the PADP plot. Thus the corresponding settings were used for collecting the data for the neural network.

As seen in Figure 9 the setting with 4 bounces were enough for rays to reach the human and the receiving antenna. The image is simplified and most rays are removed for increased visibility. In the actual simulation the transmitting antenna (Tx) will transmit signal that will illuminate the room and rays are seen all over the image.

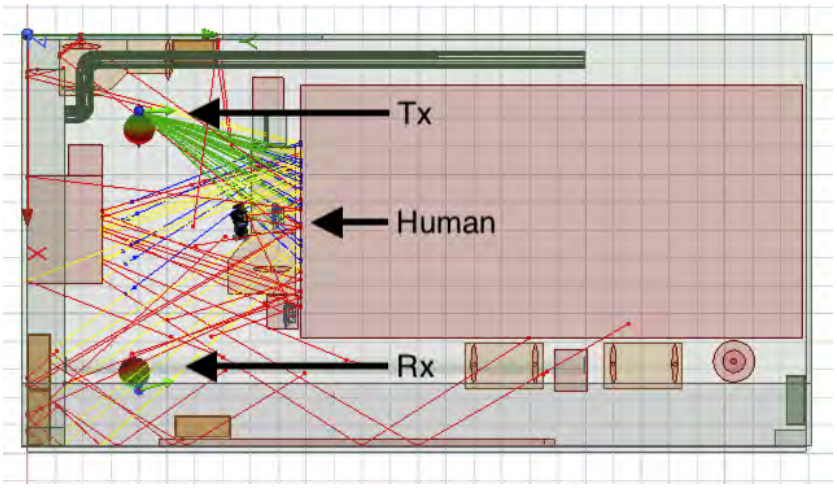

Figure 9: Rays bouncing between the transmitting antenna (Tx) and the receiving antenna (Rx). Green is the first path, blue second, yellow third, and red fourth and fifth.

To increase the efficiency and to be able to run the simulation over several days without interruption, several measurement setups were prepared in advance. This was made using the parameter sweep function in HFSS. By assigning a coordinate system to each antenna and the human model, it was possible to move all objects in x, y, z, φ and θ direction (as in spherical coordinates). For each configuration, a sweep across the frequency range of 4–30 GHz was conducted, along with a 360-degree rotation of the receiving antenna in 15-degree steps to enable comparison between the PADPs of the simulation and the lab measurements. For the dataset used in neural network training, a reduced angular range of 45 degrees with 15-degree steps was used to minimize simulation time.

3.3.1 Materials

To be able to simulate how the transmitted signal was reflected on the different structures and furniture in the lab, all items were assigned to different materials from the HFSS library. As seen in figure 6 all items were color coded with corresponding materials. red for metal, orange for wood, and blue for glass. The human model was also sourced from the HFSS library and was primarily composed of salt water to approximate human tissue properties.

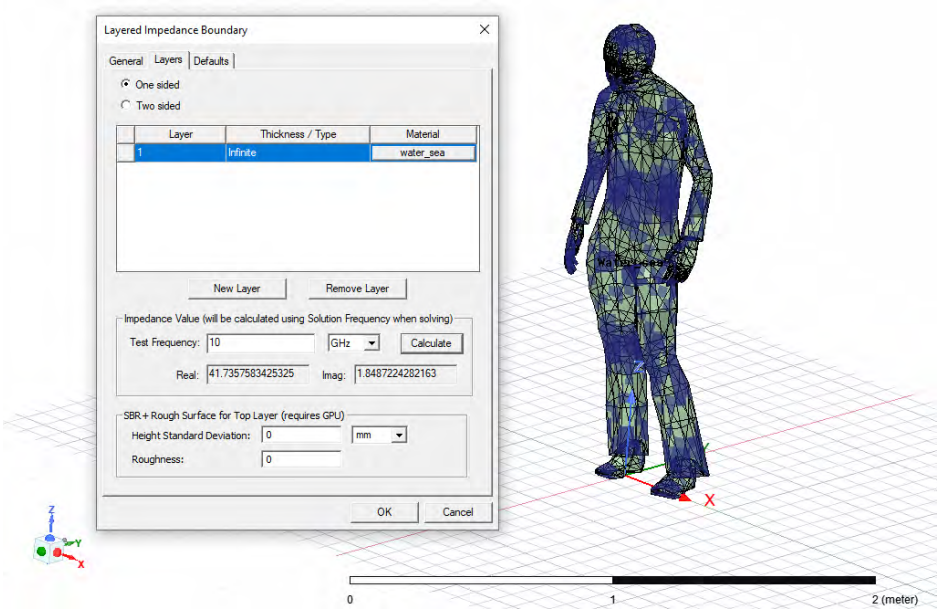

Figure 10: Close up on the simulated human and the settings on the model in HFSS.

As seen in figure 10, the human model consists of numerous small geometric components arranged at various angles to emulate realistic signal reflections from a human body. The surface of the human model was approximated as a one sided impedance layer. That means that only the reflection of the signal that hit the surface was included in the calculations and the remaining radiation that entered the model was neglected. The reflection of the human surface was dependent on the permittivity which in turn is dependent on frequency. To correctly represent the human reflection, the impedance value was calculated for the whole frequency sweep. As a sample value 10 GHz generated an impedance value of $Z = 41.7 + 1.85j\ \Omega$.

In addition to metal, glass, and wood, the simulation model also incorporates concrete and plastic. Table 2 summarizes the electromagnetic and physical properties assigned to each material. These values are based on HFSS library defaults, which are approximations; in particular, metallic surfaces are modeled as perfect electric conductors (PEC), meaning they reflect all energy.

Table 2: Material properties used in the simulation (units omitted as shown in the software).

Material	Relative Permittivity	Relative Permeability	Bulk Conductivity	Dielectric Loss Tangent	Mass Density
Concrete	2.84605	1	9.97E−12	0.0158114	2481.93
Glass	5.5	1	0	0	2500
Metal (PEC)	1	1	1.00E+30	0	0
Plastic	2.99333	1	1.00E−14	0.00591618	1029.81
Wood	7.34281	1	9.12E−07	0.0860814	666.333

3.3.2 Antenna characteristics

The antennas that were used for physical measurements were measured in an anechoic chamber to get the radiation pattern (see Figure 11). Antenna radiation patterns were defined in HFSS as the angle where the main lobe lost 3 dB of the signal. This resulted in a vertical beam width of 40° and a horizontal beam width of 50°. The match port impediance was set to 50 Ω.

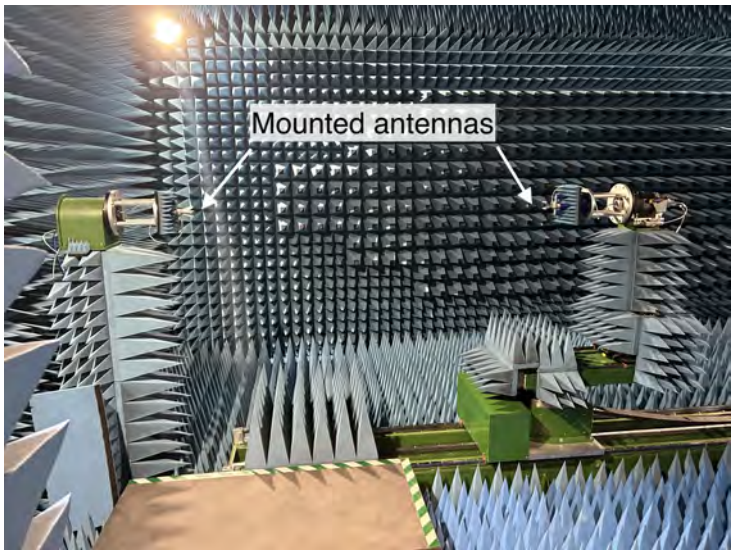

Figure 11: Measurement of the far-field characteristics of both antennas.

Using the formula $2 \cdot \frac{D^2}{\lambda}$ = far-field, the minimum far-field distance was calculated. That distance was much smaller than the length of the chamber which allowed for far-field measurements. In the formula "D" is the width of the opening of the horn antenna and λ is the wave length of the test signal.

3.4 Criteria for frequency bands to be recommended

Once measurements were made the results of different frequency bands were compared to provide a recommendation. The main factor that was considered was the PADP which visualizes the transmission (S_{21}) parameter. Visual analysis of the graphs allows for comparison of loss, the amount of noise and the clarity of the main multipath components. Little loss, little noise, and clearly distinguishable signal features were desired.

3.5 Structure of neural network

The network consists of three fully connected layers. The input layer is a flattened version of the S_{21} matrix, which has $frequency\ points \cdot anglesteps = 2601 \cdot 3 = 7803$ points. The first hidden layer has 1024 neurons and the second 512 neurons, with a final output of 2 classes. Each hidden layer is followed by a ReLU activation function and a dropout layer to prevent overfitting. The Adam optimizer is also used while training. The resulting output is a vector $\mathbf{z} = [z_0\ z_1]$.

3.6 Training of neural network

Ninety out of a hundred real life measurements were used to train the network. The last ten were later used to test the FNN. During the training, the number of epochs and learning rate were modified to find values that makes the FNN as confident as possible.

A similar approach was used when training with the simulated data, where the majority was used for training while saving a small part for inference to be able to properly assess the network's capabilities.

4 Result

In this section, the main results of this project are presented.

4.1 Link budget

Figure 12 below showcases the theoretical free space path loss (FSPL) versus measured FSPL for the setup. The theoretical values are calculated according to equation 2 and the measured path loss is data from a basic LOS setup.

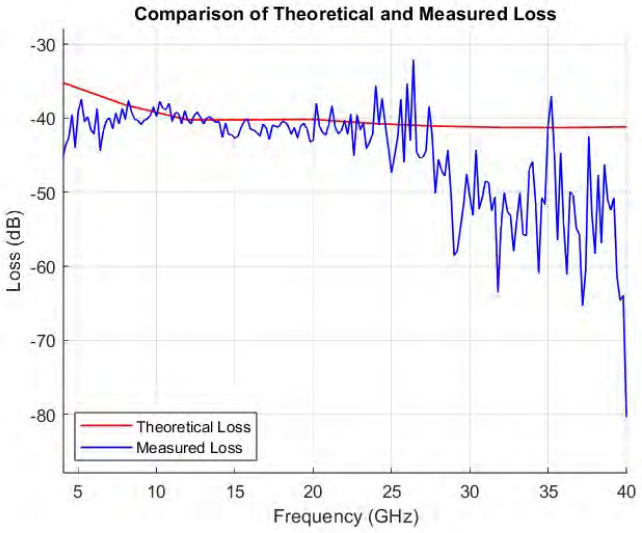

Figure 12: Expected vs Measured path loss

4.2 PADPs

The difference between the first (13a) and a refined version (13b) of a PADP plot can be seen in figure 13. Dynamic range and color was chosen to increase visual clarity.

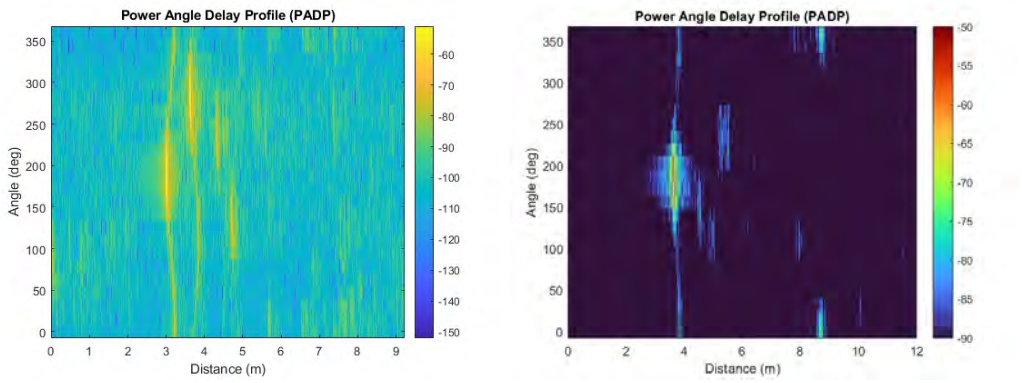

(a) First PADP (b) Refined PADP

Figure 13: Power Angle Delay Profiles at different stages of the project

In the PADPs the horisontal axis represents the covered distance, vertical axis represents the angle of arrival and the color map represents the signal strenght expressed in dB.

4.2.1 Visualization of human detection

Figure 14 shows an example of how a human could appear in a PADP.

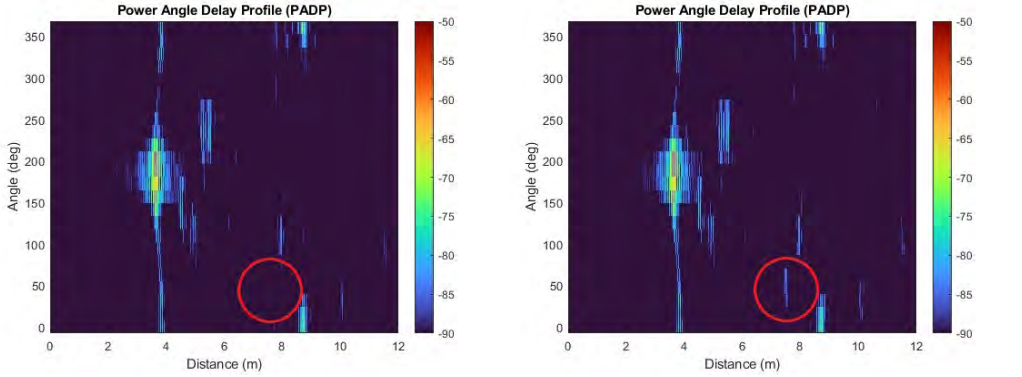

(a) No human (b) Human

Figure 14: Comparison between human presence and absence

The main difference in the PADP with and without human is an additional reflection from the human which appears as a power peak. This is highlighted in the red circle.

Figure 15 below shows an example of how a human could appear in a PADP from the simulation.

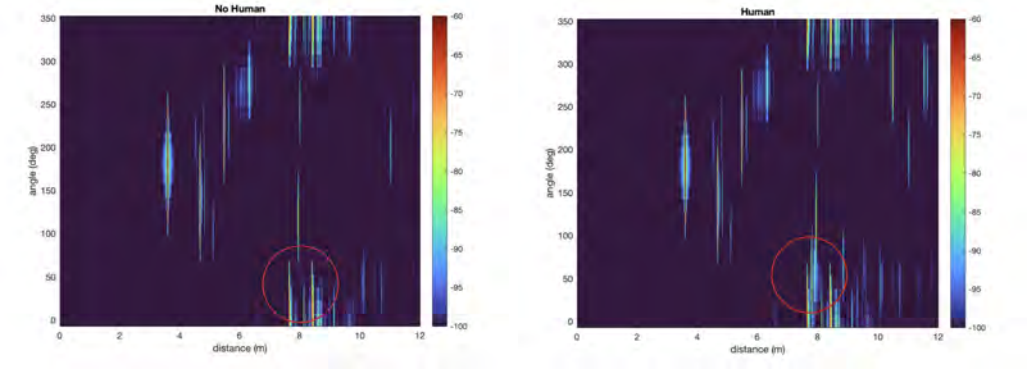

(a) No human (b) Human

Figure 15: Comparison between human presence and absence in simulation

The PADPSs in figure 15 is the simulated variation of the PADPs in figure 14. Similarly to figure 14, the red circle highlights the reflection from the simulated human. Noted that the dynamic range differers in the simulated case. The simulated variation has a larger dynamic range, where the power ranges from -100 to -60 dB while the measured data ranges from -90 to -50 dB.

4.3 Frequency slicing

4.3.1 Frequency slicing on lab measurement data

Frequency slicing on the lab measurement data was made for LOS and NLOS as seen in figure 16 and figure 18. The datasets were sliced into low, medium and high frequency slices with 0.4 GHz bandwidths at 5, 14 and 26 GHz for both LOS and NLOS.

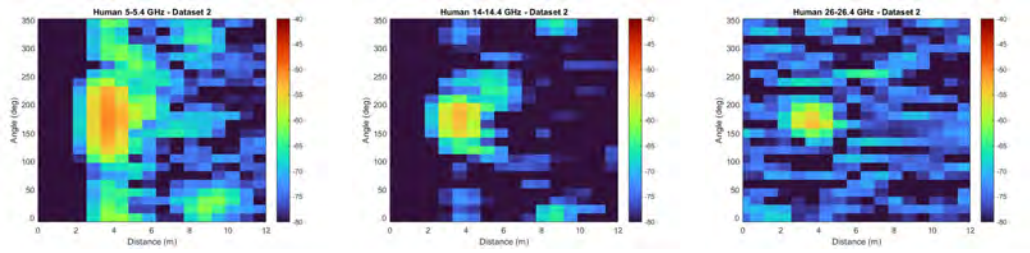

(a) 5 - 5.4 GHz (b) 14 - 14.4 GHz (c) 26 - 26.4 GHz

Figure 16: Power Angle Delay Profiles at different frequency bands for LOS

The main differences of the properties of different frequency bands are visualised in figure 16. In regards to the SNR, it gets lower with increasing frequency. It is also clear that some of the main features are lost in both the middle and high frequency slices.

The radiation patterns of the antennas at different frequencies were measured in the lab and the result can be seen in figure 17.

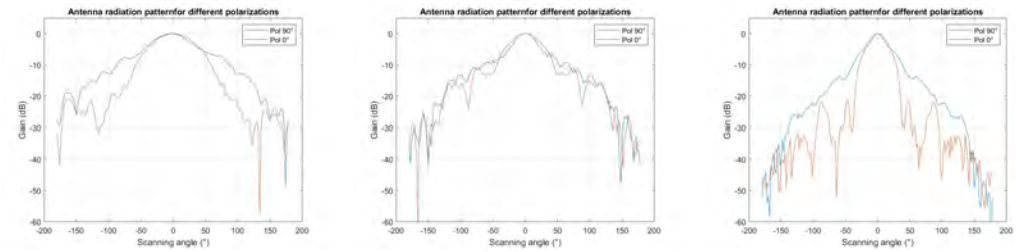

(a) 5 GHz (b) 14 GHz (c) 26 GHz

Figure 17: Corresponding antenna radiation pattern at different frequencies.

The radiation pattern for the transmitting antenna for different parts of the frequency band is plotted in figure 17. The blue graph represents the vertically polarized antenna measurement and the red graph represents the horizontal variation. The antenna gain is normalized so that the highest gain is equal to 0 dB. It can be seen that the beamwidth gets narrower as the frequency increases.

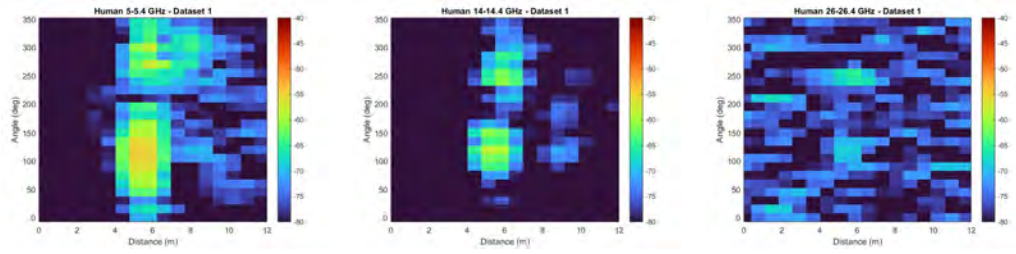

(a) 5 - 5.4 GHz (b) 14 - 14.4 GHz (c) 26 - 26.4 GHz

Figure 18: Power Angle Delay Profiles at different frequency bands for NLOS

The frequency slicing that is visualized in 18 is similar to the slicing that is presented in figure 16. The difference is that the prior is constructed from NLOS data. A consequence of the NLOS case is lower power intensity of the received signal.

4.3.2 Frequency slicing on simulated data

Frequency slicing on the simulated data was made for LOS as seen in figure 19.

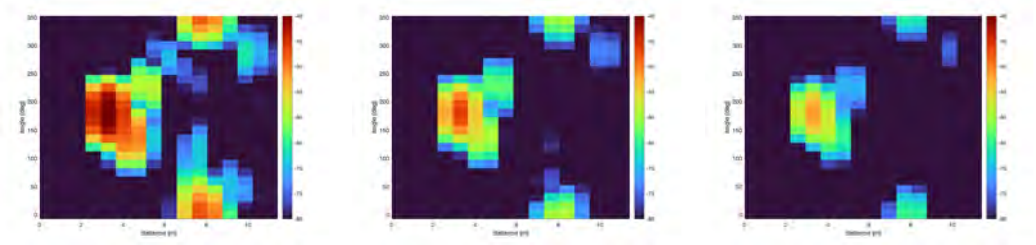

(a) 5 - 5.4 GHz (b) 14 - 14.4 GHz (c) 26 - 26.4 GHz

Figure 19: Power Angle Delay Profiles at different frequency bands for Simulated LOS measurement with a human.

In the sliced PADPs the received signal strenght decreases with increasing frequency.

4.4 Human presence detection using neural network

The human presence detection results for the simulation and the lab measurements using a neural network are presented below. The confidence of classifications are calculated using the $softmax$ function. This function converts the vector outputs from the neural network into probabilities according to equation 11. Since the calculation based on exponentials, the probability can never equal zero, or one hundred percent for any class. Therefore, any such probabilities presented below are rounded up.

$$softmax(z_j) = \frac{e^{z_j}}{\sum_{i=0}^{n} e^{z_i}}, \ \mathbf{z} = [z_0 \ z_1] \tag{11}$$

Table 3 displays resulting confidence when training the neural network purely with the simplified lab measurements mentioned in section 3.1.2. The percentages shown are the average confidence of 5 inferences of the network, for both human and non-human situations. The measurements were done to be able to optimize the settings for the neural network.

Table 3: Confidence depending on learning rate and epochs

Learning Rate (LR)	**Epochs**	**Human (%)**	**No-Human (%)**
1e-05	10	50.55	51.50
1e-05	20	63.26	53.01
1e-05	30	84.80	56.47
1e-05	40	95.51	54.58
1e-04	10	99.44	51.50
1e-04	20	99.91	69.07
1e-04	30	99.98	70.39
1e-04	40	99.99	65.65
5e-04	10	99.98	64.50
5e-04	20	100.00	79.29
5e-04	30	100.00	74.85
5e-04	40	100.00	93.71
1e-03	10	99.98	80.60
1e-03	20	100.00	83.46
1e-03	30	100.00	92.01
1e-03	40	100.00	84.33
5e-03	10	99.82	78.18
5e-03	20	99.99	69.58
5e-03	30	50.56	50.56
5e-03	40	100.00	70.11

Table 4 shows the results from training the neural network using different combinations of training and test datasets, either from simulated data, laboratory measurements, or a combination of both. The confidence and variance were calculated based on multiple training runs using data that had not been included in the training process. Testing has been performed as in Table 3 to optimize the settings for the learning rate and number of epochs.

Table 4: Results from the Neural network with different environments

Training Data	Test Data	No. of Epoch	Learning rate (%)	Confidence (%)	Variance
Lab	Lab Human	6	5e-4	99.78	0.0587
Lab	Lab No Human	6	5e-4	98.90	8.0316
Sim	Sim Human	6	5e-4	99.99	0.000001006
Sim	Sim No Human	6	5e-4	99.97	0.001798
Lab + Sim	Lab Human	6	5e-4	99.72	0.5632
Lab + Sim	Lab No Human	6	5e-4	99.92	0.0648
Lab + Sim	Sim Human	6	5e-4	99.99	0.00004182
Lab + Sim	Sim No Human	6	5e-4	99.84	0.1566
Lab	Lab Human	22	5e-4	99.99	0.00004538
Lab	Lab No Human	22	5e-4	99.99	0.0002415
Sim	Lab Human	6	5e-4	3.10	-
Sim	Lab No Human	6	5e-4	96.98	-
Lab	Sim Human	6	5e-4	77.52	-
Lab	Sim No Human	6	5e-4	21.60	-

5 Discussion

This section provides a critical analysis of the main results, exploring their implications, limitations, and potential for future development.

5.1 Lab measurements

The comparison between expected and measured free space path loss (FSPL) as seen in figure 12 revealed a consistent offset, which likely results from practical imperfections such as cable loss and reflections in the lab environment. In particular there is a lot of loss at higher frequencies compared to the theoretical values, likely due to limitations in the hardware. Despite calibration, minor errors in measurement setup may persist. This shows that the link budget model works well in theory, but also highlights how important it is to confirm the results with real measurements.

The point of plotting PADPs is to be able to visualize a human with the naked eye. To enhance the visualization of the first PADPs plotted as seen in figure 13, some adjustments were made. The color map was improved along with the range in the color bar to highlight the components more clearly. The resulting PADPs provided clearer insights into the dominant signal paths and reflections, making it easier to identify human-induced distortions.

Regarding the lab measurements, there was some potential sources of error that were inevitable. During most of the measurements conducted to construct the PADPs there were people present in the room apart from the test person. Thus resulting in unwanted human presence in some of the angle slices. Reflections induced by this were not prominent features in the PADPs, but they could cause disturbances in the training of the neural network. Therefore the PADP data were not used for that purpose. During all of the the lab measurements electronic communication devices were present in the room. Consequently interfering with the S_{21} data due to contributing with broadband noise. Though this may have affected measurements, the neural network was still able to distinguish human presence, and the PADPs contain all main features expected.

5.2 Simulation

When comparing LOS measurements done in the lab (Figure 16) compared to the simulation (Figure 19), both the amplitude of the received signal and the signal to noise ratio differs significantly. The simulated data does not contain noise and the maximum number of bounces are set to 4 which means that the signal will suddenly disappear after 4 bounces. This result in a very clear image quite different from the real lab measurements. However, the main reflections are present and a human can be seen. A big difference is the amplitude of the received signal. One reason for this could be the approximations of the materials in the simulation. For example is metal approximated as a perfect electric conductor which means that it reflects 100% of the signal. In reality there were very few objects in the lab that were only made of metal and the would probably not reflect the signal in the same way.

One of the differences in the PADP plots is that the main reflection is broader in the angle domain in the measurement compared to the simulation. That could be because the antennas used in lab measurement have side lobes seen in Figure 17 compared to the simplified antenna model used in the simulation. As they were defined as described in section 3.3.2, they have no side lobes and will therefore have a narrower reflection seen in fewer number of angles.

As described in Section 3.2 the interior of the digital twin was constrained to large objects. Smaller objects in shelves and handles and details on furniture were neglected. This was done due to the assumption that a higher frequency than 30 GHz was needed to be able to see that level of detail in the PADPs. It might be hard in general to evaluate small details in the PADPs and assess what they represent in reality. After the processing of the data, only amplitude, distance and receiving angle are presented and it would be hard to know if a reflection comes from a small detail or from the larger object the detail was attached to.

One of the main reasons for doing a twin was to evaluate if the simulation worked relative to the lab measurements. While the main features are the same for both, there is still some further refinement to be done with the simulation to make it representative of real life. One potential advantage with the differences however is that if the simulation and lab measurements are not exactly equal, training the neural network with both types of data would make the network less specialized, and in theory it may perform better in general cases. This has however not been tested.

The main limitation from the result of the simulation and the result from the neural network trained with it's data, is that it is not clear if the simulation actually improves the model. Even though this could be due to the lack of normalizing the data between simulation and real world measurements it could also be a consequence of the lack of accuracy or noise. The limited amount of bounces and ray density could have produced a result too far from reality. More research can be done to evaluate the best process to normalize the data and to see if there are other ways to acquire a reasonable simulation time without sacrificing accuracy in therms of bounces and ray density. Another limitation in the simulation is that it is a model of a relatively small room. Increasing the size of the model and introducing other materials and setups might be a good choice to increase the quality of the neural network. In the case of this report, all measurements and simulation have been done in the same environment and there is a risk that the neural network would only work with tested data from this environment. Therefore, future research is needed to extend the dataset to a wider range of setups and environments.

Many of the decisions regarding the simulation accuracy were a direct consequence of the time it took to execute one simulated setup. The project had limited access to a server with high processing power and most simulations in the beginning of the project (made on a slower server) took long enough to finish that real world measurements was a more efficient way of collecting data. This raised the question if a simulation actually help to collect data for a neural network. However, the access to a better server enabled to collect 350 setups with and 350 setups without a human. This was considered a good amount compared to the real world measurements that was 50 setups of each measurement.

Simulations were performed using the same setup but with varying ray densities to determine the optimal configuration for subsequent runs, as described in Section 3.3. A ray tracing plot was also generated to visualize the number of bounces. These plots was analyzed to evaluate how changes in ray density affect the results. The human subject remained clearly visible even at lower ray densities; therefore, the ray density was reduced to decrease simulation time while still enabling the collection of a significant amount of data.

5.3 Neural network

The neural network achieved high accuracy when trained and tested on data from the same environment. This indicates that the model effectively learned to recognize patterns in the S_{21} parameter data that correlate with human presence. A network trained on a combination of both measured and simulated data also achieved high confidence when tested on both types of data.

However, as shown in Table 4, a significant performance drop occurred when the model was tested on data from an environment different from that on which it was trained. In one case, the network trained on simulated data and tested on measured data consistently predicted the presence of a human, even when none was present. In contrast, a network trained on measured data and tested on simulated data failed to detect a human entirely. The probable reason is that there were differences in the simulated and measured data and a possible solution to that could be to normalize the data to make the different environments more alike without affecting patterns in the data. When the network is trained with both datasets, the network is able to handle the difference between them and correctly tell if there is a human or not. A possible explanation could also be that the human model used in the simulation differs from a real human, and the corresponding reflections were to different for the neural network to understand.

The variance in the network's confidence was higher when trained and tested only on measured data compared to when simulated data was included in the test set. While increasing the number of training epochs could reduce this variance, it may also lead to overfitting, resulting in a less generalized model that performs poorly on previously unseen data.

5.4 Frequency slicing

Frequency slicing revealed clear differences in signal propagation characteristics for LOS measurements. Only the higher frequency PADP exhibits clear noise before the 2-meter mark as seen in figure 16 which are absent in the lower frequency PADPs. However, all three images show signals that could be mistakenly interpreted as noise after the two meter mark. The absence of any such readings before two meters however means that it is caused by reflections from the surrounding room or environment, not background noise. With this in mind, high frequencies do not seem suitable in this specific situation and project.

On the other hand, at higher frequencies the main lobe of the antenna is narrower and more directional, which can be helpful for more accurate localization and better separation of signals coming from different directions. Higher frequencies also allow for wider bandwidths which indicates better time resolution and the ability to tell apart closely spaced reflections. One solution to potentially utilize higher frequencies while maintaining a strong SNR is using a higher gain antenna or simply implement the usage of amplifiers. Using a higher gain antenna or amplifiers would both boost the signal, thus improving SNR. The amplifier would increase the signal strength more than using a more directional antenna, with the trade-off of adding a little bit of noise. However, due to limitations in this project, this is left for future research.

5.5 Future research

For future research, some things could be explored further. A dynamic measurement setup would be possible at the cost of a more complex project. The S_{21} data would no longer be steady with time and instead show temporal variations with movement, like Doppler shifts. Doppler shifts occur due to motion-induced changes in frequency. These changes could be used to estimate human movements, velocity and direction. This opens the possibility for the neural network to find movement of the human, like breathing or walking, and not just presence. The combination of presence and specific human movement could make the neural network more confident in classifying a human. A dynamic situation, however, would be harder to simulate and would require a more advanced neural network and measurement setup.

Future research on static situations could be to improve the neural network, collect more data and fine-tune the simulator. A normalization processing strategy for the simulations could make the datasets more similar to the real-life measurements. This could make the neural network more confident despite training or testing on simulation or real-life datasets.

6 Ethical aspects

When examining wireless channels for communication and the ability to detect people through these channels, the issue of privacy arises. This form of detection can be seen as a form of surveillance and therefore a breach of privacy. Compared to other popular means of presence detection such as cameras or radar however, detecting through communication channels has notable advantages. Compared to cameras this method would be far less invasive since it would not be able to identify a person on its own. The advantage compared to radar is that you do not need the same amount of equipment since the communications part of a vehicle and other "already-installed" communication equipment would be all you need. Furthermore you would be able to communicate and detect people using the same frequencies which would mean that the frequencies that vehicle radars currently use would be available for other uses, which makes it more sustainable than radar.

Despite not being very invasive on its own, the ability to detect persons may also be combined with other communication methods such as the mast communicating with the individual's phone. This could provide a more precise position and opportunity to identify the individual. This creates a situation where a mast not only detects a human but also knows their exact location and potentially their identity.

7 Conclusion

One of the goals of the project was to recommend five frequency bands for indoor 6G. However, due to gradual changes in amplitude and features over the frequency span it was more practical to divide the whole spectrum into three parts and look into a small span in every section. The chosen span would then be the one with highest SNR while still including all the main multi-path features. The recommendation would be 5-5.4 GHz according to the result of this project. The middle frequency band is ruled out due to it losing some features of the signal. Higher frequencies were not effective due to poor SNR, which made it difficult to distinguish the presence of a human. The higher frequencies do however have advantages in potential information rates and angular resolution which may still make them interesting for further research.

A digital twin of the Chalmers antenna lab was constructed and simulations were performed like the measurement and PADP where compared and regardless of some differences the main features like shelves, desks and walls were similar in PADP from both measured and simulated data.

Even though the simulation could output usable data and the fact that a human could be observed both in the PADP plots and by the neural network, the data was not similar enough to reality to enable cross testing of the neural networks. When testing the lab measurement of a setup including a human on a neural network trained on exclusively simulated data, the confidence was around 3 %. This does not mean that the simulation did not work but that it is probably not similar enough to reality to be able to detect a human with the neural network trained on simulated data. As mentioned earlier, this could also be due to the lack of normalisation of the data. Overall the neural network was able to recognize a human with high precision both with trained and tested on measured and simulated data in the scenarios that were tested.

The project leaves room for future research, such as adapting the setup for higher frequencies, further refining the simulation, or exploring more advanced environments.

8 References

References

[1] Z. Zhang, X. Zhang, Y. Zhang, *et al.*, "Toward 6g wireless networks: Vision, enabling technologies, and new paradigm shifts," *IEEE Communications Surveys Tutorials*, vol. 25, no. 4, pp. 2223–2257, 2023. DOI: 10.1109/COMST.2023.3276566. [Online]. Available: https://ieeexplore.ieee.org/document/10816608.

[2] A. Ploshchyk, R. Politanskyi, and S. Haliuk, "Analysis of antenna system s-parameters in wireless communication networks using hfss: Role and significance in wi-fi and 5g," in *2024 IEEE 17th International Conference on Advanced Trends in Radioelectronics, Telecommunications and Computer Engineering (TCSET)*, 2024, pp. 560–563. DOI: 10.1109/TCSET64720.2024.10755706.

[3] G. Thomas and R. Isaacs, "Processing, storage and display of physiological measurements," *Anaesthesia*, vol. 10, no. 1, 2009, Accessed May 8, 2025. [Online]. Available: https://www.anaesthesiajournal.co.uk/article/S1472-0299(08)00285-3/fulltext.

[4] F. L. Bianco, G. Naldini, J. Amado, S. Chiale, and F. Gonzalez, "Measurement module s parameters for vector network analyzer," *IEEE Latin America Transactions*, vol. 11, no. 1, 236 – 241, 2013. DOI: 10.1109/TLA.2013.6502809. [Online]. Available: https://www.scopus.com/inward/record.uri?eid=2-s2.0-84876793918&doi=10.1109%2fTLA.2013.6502809&partnerID=40&md5=c05687d31a893ad8dbcb7a764c784648.

[5] M. Hiebel, "Vector network analyzer (vna) calibration: The basics," Rohde & Schwarz, White Paper, 2008, Accessed: 2025-05-05. [Online]. Available: https://www.rohde-schwarz.com.

[6] Ansys. "What are s-parameters?" Accessed: 2025-04-25. (2024), [Online]. Available: https://www.ansys.com/simulation-topics/what-are-s-parameters.

[7] C. Özdemir, *Inverse Synthetic Aperture Radar Imaging with MATLAB Algorithms*. Hoboken, New Jersey: John Wiley & Sons, Inc., 2012.

[8] Y. Hu, *Fourier analysis*, Lecture notes, 2020. [Online]. Available: https://youjunhu.wordpress.com/wp-content/uploads/2020/12/fourier_analysis.pdf.

[9] S. Wei, X. Ma, and J. Wang, "Experimental teaching reform of window function design in digital signal processing course," in *2022 Asia Conference on Algorithms, Computing and Machine Learning (CACML)*, IEEE, 2022, pp. 385–390.

[10] K. M. M. Prabhu, *Window Functions and Their Applications in Signal Processing*. Boca Raton, FL: CRC Press, 2014, Open access under CC BY-NC-ND 4.0, ISBN: 9781466515840. DOI: 10.1201/9781315216386. [Online]. Available: https://library.oapen.org/handle/20.500.12657/41686.

[11] J. Li, X. Zhu, and Y. Wang, "Sar image despeckling using a convolutional neural network," in *2018 IEEE International Geoscience and Remote Sensing Symposium (IGARSS)*, IEEE, 2018, pp. 1234–1237. DOI: 10.1109/IGARSS.2018.8423070. [Online]. Available: https://ieeexplore.ieee.org/document/8423070.

[12] Z. Li, W. Du, Y. Zheng, *et al.*, "Precise power delay profiling with commodity wifi," in *Proceedings of the 21st Annual International Conference on Mobile Computing and Networking (MobiCom '15)*, New York, NY, USA: Association for Computing Machinery, 2015, pp. 53–64. DOI: 10.1145/2789168.2790124. [Online]. Available: https://dl.acm.org/doi/10.1145/2789168.2790124.

[13] S. Kollmannsberger, D. D'Angella, M. Jokeit, and L. Herrmann, *Deep Learning in Computational Mechanics: An Introductory Course* (Studies in Computational Intelligence). Springer, 2021, vol. 977, Accessed April 23, 2025, ISBN: 978-3-030-76587-3. DOI: 10.1007/978-3-030-76587-3. [Online]. Available: https://doi.org/10.1007/978-3-030-76587-3.

[14] P. H. Kazem and A. Asghar, *Neural networks*. 2024, 3 – 8, Cited by: 0. DOI: 10.1016/B978-0-443-16147-6.00017-7. [Online]. Available: https://www.scopus.com/inward/record.uri?eid=2-s2.0-85202868901&doi=10.1016%2fB978-0-443-16147-6.00017-7&partnerID=40&md5=fe111a044e9b51f2b1ca7288dfdcfba8.

[15] F. Chen, Y. Zhang, and M. G. Amin, "Indoor human detection and ranging using uwb radar and artificial neural network," *IEEE Sensors Journal*, vol. 18, no. 23, pp. 9721–9731, 2018. DOI: 10.1109/JSEN.2017.2786080.

[16] D. P. Kingma and J. Ba, "Adam: A Method for Stochastic Optimization," *International Conference on Learning Representations (ICLR)*, 2015, arXiv:1412.6980. [Online]. Available: https://arxiv.org/abs/1412.6980.

[17] F. Gatti, "Artificial neural networks: Basic architectures and training strategies," in Accessed via Scopus, 23 April 2025, John Wiley & Sons, 2024, pp. 185–275. DOI: 10.1002/9781394325665.ch5. [Online]. Available: https://www.scopus.com/inward/record.uri?eid=2-s2.0-85208867010&doi=10.1002%2f9781394325665.ch5&partnerID=40&md5=b94072248eeb569bd826d9dc7d6bf2eb.

[18] I. Goodfellow, Y. Bengio, and A. Courville, *Deep Learning*. MIT Press, 2016, http://www.deeplearningbook.org.

[19] A. Paszke, S. Gross, F. Massa, *et al.*, "Pytorch: An imperative style, high-performance deep learning library," Cited by: 29810, vol. 32, 2019. [Online]. Available: https://www.scopus.com/inward/record.uri?eid=2-s2.0-85090176877&partnerID=40&md5=b8ecd177286b903fcb2493893027cce0.

[20] *ANSYS HFSS SBR+: Installed antenna applications*, Available: https://www.ansys.com, ANSYS, Inc., Canonsburg, PA, 2018.